HHS Public Access

Author manuscript

IEEE Trans Biomed Eng. Author manuscript; available in PMC 2022 December 05.

Published in final edited form as:

IEEE Trans Biomed Eng. 2021 August ; 68(8): 2563–2573. doi:10.1109/TBME.2021.3055777.

–Design of an Intraoral Dipole Antenna for Dental Applications

Ali Caglar Özen [Member, IEEE],
Department of Radiology, Medical Physics, Medical Center – University of Freiburg, Faculty of Medicine, University of Freiburg, 79085 Freiburg, Germany

German Consortium for Translational Cancer Research Partner Site Freiburg, German Cancer Research Center (DKFZ), 69120 Heidelberg, Germany

Division of TMD & Orofacial Pain, School of Dentistry, University of Minnesota, Minneapolis, MN 55402 USA

Djaudat Idiyatullin,
Center for Magnetic Resonance Research and Department of Radiology, University of Minnesota.

Gregor Adriany,
Center for Magnetic Resonance Research and Department of Radiology, University of Minnesota.

Steve Jungst,
Center for Magnetic Resonance Research and Department of Radiology, University of Minnesota.

Naoharu Kobayashi,
Center for Magnetic Resonance Research and Department of Radiology, University of Minnesota.

Beth R. Groenke,
Division of TMD & Orofacial Pain, School of Dentistry, University of Minnesota.

Michael Bock,
Department of Radiology, Medical Physics, Medical Center – University of Freiburg, Faculty of Medicine, University of Freiburg.

Michael Garwood,
Center for Magnetic Resonance Research and Department of Radiology, University of Minnesota.

Donald R. Nixdorf
Division of TMD & Orofacial Pain, School of Dentistry, University of Minnesota

Department of Neurology and Radiology, Medical School, University of Minnesota.

Abstract

Objective: In dental MRI, intraoral coils provide higher signal-to-noise ratio (SNR) than coils placed outside the mouth. This study aims to design an intraoral dipole antenna and demonstrates the feasibility of combining it with an extraoral coil.

Corresponding author: Ali Caglar Özen. a.oezen@uniklinikfreiburg.de.

This article has supplementary downloadable material available at https://doi.org/10.1109/TBME.2021.3055777, provided by the authors.

Digital Object Identifier 10.1109/TBME.2021.3055777

Methods: Dipole antenna design was chosen over loop design, as it is open toward the distal; therefore, it does not restrain tongue movement. The dipole design offers also an increased depth-of-sensitivity that allows for MRI of dental roots. Different dipole antenna designs were simulated using a finite-difference-time-domain approach. Ribbon, wire, and multi-wire arms were compared. The best design was improved further by covering the ends of the dipole arms with a high-permittivity material. Phantom and in vivo measurements were conducted on a 3T clinical MRI system.

Results: The best transmit efficiency and homogeneity was achieved with a multi-wire curved dipole antenna with 7 wires for each arm. With an additional high-permittivity cap the transmit field inhomogeneity was further reduced from 20% to 5% along the dipole arm. When combined with extraoral flexible surface-coil, the coupling between the coils was less than −32dB and SNR was increased.

Conclusion: Using intraoral dipole design instead of loop improves patient comfort. We demonstrated feasibility of the intraoral dipole combined with an extraoral flexible coil-array for dental MRI. Dipole antenna enabled decreasing imaging field-of-view, and reduced the prevalent signal from tongue.

Significance: This study highlights the advantages and the main challenges of the intraoral RF coils and describes a novel RF coil that addresses those challenges.

Index Terms—

Dental MRI; Dipole Antenna; Intraoral Coil; Magnetic Resonance Imaging; Radiofrequency Coil

I. Introduction

IN CLINICAL practice, imaging of the teeth and the surrounding tissue is usually performed with digital two-dimensional radiography, multi-detector computed tomography (MDCT), or cone-beam CT (CBCT) [1]–[3]. The potential of dental MRI was already discussed in 1981 [4], as MRI does not use ionizing radiation and offers excellent and adjustable contrast, but it has been clinically implemented only in the recent years due to the increasing number of applications where high resolution soft tissue contrast is needed, and because it is becoming technically and economically more feasible. The feasibility and advantages of dental MRI have been demonstrated in various applications including: pre-surgical planning, implant planning, assessment of dental and periapical anatomy and pathology, localization of impacted teeth, evaluation of dental vitality, tumor detection, and imaging of the morphology and function of the temporomandibular joint [5], [6], [15]–[20], [7]–[14].

Dental MRI is also potentially useful for investigating hard tissues, such as cortical bone and dentin [21], [22]. Unfortunately, in bone the rapid decay of the MR signal requires an increase in the encoding bandwidth. For bone MRI FID-based imaging methods have been proposed, which are limited by finite acquisition delays, i.e., dead time, and bandwidth due to limited radio frequency (RF) power amplifier performance, and the gradient slew rates (for reviews and comparison [23]–[28]). Imaging techniques, such as SWIFT and its variations, use a frequency-modulated excitation and a simultaneous acquisition to acquire signal from tissues with very short T2 or T2* [29]–[34]. All these pulse sequences are based

on radial encoding, and cannot use sliceor slab-selective pulses to preserve signal from tissues with ultra-short T2. Thus, the acquired field-of-view (FOV) must include the entire sensitive volume of the RF coil to avoid aliasing. The resolution of an image voxel depends on the FOV and the reconstructed matrix size. Increased FOV results in highly increased scan times to achieve the desired image resolution with similar SNR [35]. Therefore, to achieve higher resolution in reasonable scan times, smaller and more localized RF coils must be used.

The SNR provided by a coil is essentially proportional to the geometric filling factor, η, which is a measure of the fraction of the RF coil volume occupied by the sample; and the quality factor, Q, of the coil [36].Although there is a clinical need for dental MRI, and advanced short-T2*-sensitive pulse sequences for bone imaging can be implemented in most of the clinical MRI systems, commercially available RF coils are often not compatible with the dental anatomy. A coil configured to provide a limited and sculpted FOV is highly desirable to solve this problem.

In dental MRI, submillimeter structures (e.g., small fractures within dental roots) must be resolved. To achieve this high resolution within clinically acceptable measurement times, the imaging FOV must be restricted to the target region which can be realized by a small RF excitation field, B_1^+, a limited receive sensitivity B_1, or a combination of both. So far mainly extraoral surface coils and coil arrays have been used [37]–[39]. For an average-sized patient, the distance between an extraoral coil element and a molar tooth is about 30–50 mm, which reduces the sensitivity significantly. In addition, with an extraoral configuration, the cheek and buccal fat produce intense signal. As a result, the signal from these unwanted tissues dominates the images. To overcome this limitation an intraoral coil was proposed that is positioned between the teeth and cheek, i.e., in the buccal vestibule which increases both resolution and SNR [40]. By sacrificing patient comfort, as well as SNR, the intense signal from the cheek could be eliminated in a similar intraoral configuration with shielding [41]. In [42], an inductively coupled intraoral coil was developed. The inductively coupled coils were designed to image a single tooth and to be used with external coil elements. However, the tuning of the coil for each patient is challenging, as it cannot be modified once the coil is sealed. Furthermore, these coils can only acquire MR signal from the apices of posterior teeth due to anatomical constraints.

For better coverage and patient comfort, an intraoral loop coil with the coil plane orthogonal to B_0 was developed, where the transverse B_1 fields are sensitive to MR signal [43]. In most standard uses of surface loop coils, the coil plane is oriented parallel to B_0, and B_1 field components orthogonal to the coil plane are used for RF excitation and detection, whereas in [43], the unconventional placement of the loop coil intraorally and orthogonal to B_0, resulted in transverse components of B_1 which were effectively used for imaging of teeth and associated structures. The sensitive volume of the loop coil included the most important dental structures, such as the teeth and jaws, and mostly excluded cheeks and lips. However, the sensitive depth did not reach the root apices of molar teeth, and the loop obstructed the tongue movement resulting in patient discomfort. Although there are standard dental procedures where the tongue is restricted, the patient is always supervised regarding

gagging and management of saliva. Nevertheless, during MRI measurements, patients are not supervised and the dipole antenna design, proposed below, is advantageous because it does not have the posterior component restricting the tongue.

In this study, we developed a novel intraoral dipole antenna and improved its performance based on the B_1 field simulations. The coil was designed to achieve a high transmit field homogeneity and penetration depth to be able to image the dental roots. For the best-performing dipole, a prototype was constructed and compared to the reference loop coil in phantom and in vivo measurements. The dipole was also combined with a flexible surface coil receive (Rx) array to increase sensitivity.

II. Methods

A new intraoral coil design was realized with the following target features: the new coil should allow for tongue movements which are impossible with a loop design, it should provide a uniform sensitivity over the teeth and surrounding tissues, it should have a penetration depth which allows sensitive detection of the signal from dental roots, and it should minimize coil coupling with exterior Rx coil elements. A dipole design was chosen, and different dipole designs were simulated using an electromagnetic (EM) simulation tool based on finite-difference-time-domain (FDTD) approach (Sim4Life v5.0, ZMT, Zurich, Switzerland). The prototype coils were tested on a clinical 3T MRI system (Prisma, Siemens, Erlangen, Germany) in a homogeneous phantom and a human volunteer.

A. FDTD Simulations

5 dipoles with planar structure (Fig. 1(b)–(f)) and 8 with multi-planar structure (5 of which are shown in Fig. 2(a)–(e)) were designed based on average human adult mandibular dimensions [44]. A list of the dipoles is given in Table I. For comparison, the loop coil in [43] was modeled as the reference coil (Fig. 1(a)). The size of the dipole is not a free design parameter, because of the fixed size of the dental arch. In our design, we chose a size that corresponds to size “M” impression tray, which is a commonly used size for adults in the USA. This size also fits the Duke anatomical model. The loop and the dipoles have the same footprint, i.e., width of 60 mm. The dipole arms are formed either by a 10 mm-wide ribbon, a single wire (Ø1.2 mm), or multiple wires separated by 5 mm. Multi-planar dipoles have additional wires (Ø1.2 mm) at a distance of 8.6 mm to the central plane. Total length of the wire and ribbon dipoles are 123 mm, except the meandered wire, which is 188 mm-long. The resonant length of a half-wave dipole immersed inside a medium of $\varepsilon_r = 78$ would be 138 mm. To increase the effective wavelength of the dipole, tuning inductors are used as shown in Fig. 1.

The transmit field $B_1^+(x, y, z)$ efficiency, i.e., transmit field amplitude over conducted input power, B_1^+/P_{in}, were compared between the reference loop coil and dipole antennae with arms formed by ribbon, wire, meandered wire, and multiple wires in parallel with open and shorted ends (Fig. 1(a)–(f)). In all simulations, the direction of the static field B_0 is assumed to be in z direction. Tuning was achieved by a parallel capacitance, and series inductance for the loop and the dipoles, respectively (Fig. 1). Tuning inductance required for ribbon

and single-wire dipoles are 116 nH and 226 nH, respectively. Meandered wire required 168 nH inductance due to the longer conductor compared to single wire, as expected. 3-wire dipole required 93 nH, whereas multi-planar dipoles required only around 40 nH. Shorted-ends did not change the resonant length significantly, whereas multi-planar dipoles with high-permittivity cap at the ends required only 15 nH for tuning. Impedance matching was done by adjusting the input impedance of the edge source defined between the poles of the input port.

To assess the field homogeneity of the coils, the transmit efficiency was plotted along a curve along the center of the coil's conductor. This curve covers a full circular path that starts at the feed port of the coil and tracks the coil conductor in clockwise direction. Two curve profiles were extracted at transverse planes that are 10 mm and 25 mm distant from the coil (Fig. 1(a)). Note that the average human adult tooth length is 22 mm thus, the 25 mm-plane covers the apical section of the roots. The relative change of $B_1^+(z)/P_{in}$ at z_1 = 10 mm and z_2 = 25 mm was calculated as a figure of merit of the coil homogeneity. Similarly, longitudinal profiles were determined at two different levels along a line orthogonal to the coil plane (Fig. 1(a), marked as y_1 and y_2).

To increase the longitudinal depth-of-sensitivity, additional wires were added to the multiple-wire design on superior and inferior planes so that the dipole has a multi-planar structure similar to dental impression trays (Fig. 2(a)–(d)). As both the upper and the lower dental arches are imaged in dental MRI, an "H" shaped cross-section was used compared to "U" shaped cross-sections of impression trays, which cover only one arch. Again, 4 different versions of the dipoles were simulated: ribbon-based central arm, multiple-wire-based central arm, and shorted-end versions of those (Fig. 2(a)–(d)).

In general, dipole antennae have a very high impedance at the end of the arms resulting in a steep decrease in RF current. The rapid current change causes B_1^+ inhomogeneities along the dipole arms that can be reduced if a smooth transition of the impedance is set up along the arms. In [45] high dielectric constant (i.e., permittivity, ε_r) materials were attached to the end of the arms to reduce electric fields, thus to prevent tissue heating. In this study, we applied dielectric coating to improve B_1^+ homogeneity – therefore, dipole antennae were simulated with open and short-end multi-wire designs (Fig. 2(e)) where lengths of 10, 15, 20, 30 mm of the tip of the arms were coated with barium titanate ($BaTiO_3$, ε_r = 300) to study the potential increase in field homogeneity.

From all simulated designs, the most favorable design was chosen according to the highest penetration depth and field homogeneity criteria. Full simulation protocols and CAD models of the coils can be found in: https://github.com/alibaz/DentalMRI.

To ensure safe coil operation, 10g-averaged specific absorption rate (SAR_{10g}) values were simulated for the loop and the multi-planar dipole coils in homogenous phantom and the Duke anatomical model (Duke cV3.1, IT'IS Foundation, Zurich, Switzerland). The intraoral coil models were placed in the mouth of the anatomical model after slight modifications. The teeth in the upper and lower jaws of the anatomical model were shifted by 2 mm and

−2 mm, respectively, leaving a gap of 4 mm to accommodate the intraoral coil with an insulation layer of 2 mm and a total thickness of 3.2 mm. In case of overlap of the intraoral coil and the tissue (e.g., gums), a prioritization was implemented during the voxelization, where, the coil structure was set to supersede the tissue voxels. For high-permittivity cap at the end of dipole arms, $\varepsilon_r = 270$ was set.

B. Coil Construction

For the imaging experiments the best-performing design with the high-$\varepsilon_r$cap and the reference loop coil were built. The reference coil was laser-cut from a 1 mm-thick copper plate and was then soldered on a single-sided PCB for capacitive tuning and matching (Fig. 3(a), Supporting Information Fig. S1). For the dipole, a form with wire tracks was constructed from UV-cured resin using a 3D printer (Form 3, Formlabs Inc., Somerville, MA). Enameled copper wires (Ø1.2 mm) were inserted and glued within the tracks. Wires were connected at the input side of each arm, and then soldered to a single-sided PCB for inductive tuning and capacitive matching. For the implementation with a high-ε_r cap, the base form was shortened, an H-shaped hollow container was filled with $BaTiO_3$ and D_2O slurry (4:1 mixture - $\varepsilon_r = 274$ was measured with DAKS 12 – SPEAG, Zurich, Switzerland) and attached to the base form. Note that, the slurry was prepared at 40 °C, and the measured permittivity change was less than 3.6% at room temperature. The dipole arm ends were shorted by soldering short wire segments between the neighboring wires. The conducting parts were then isolated with an orthodontic resin and powder (Caulk, Dentsply Sirona Global, Charlotte, NC). Finally, the whole dipole was sealed with a silicon putty (Rapid Soft, Coltène/Whaledent AG, Altstaetten, Switzerland) (Fig. 3(b)). Photos from the construction steps are shown in Supporting Information Fig. S2. Schematics of the loop and dipole are shown in Supporting Information Fig. S1a, b.

In ultra-high field MRI the performance of dipole antennae is improved by combining them with loop receive coils [46], [47]. To apply this concept to dental MRI at high fields, a 4 channel flexible transmission line resonator (TLR, i.e., shielded loop resonators-SLR) was designed. Similar to loops and dipoles, SLRs and dipoles are geometrically decoupled when coil planes are parallel to each other. We propose to use the dipole with high-ε_r cap as the Tx element, and the SLR array as the Rx element for optimal performance. Details of the SLR design and construction can be found in Supplementary Material, Supporting Information Fig. S3.

S-parameter measurements were performed in loaded and unloaded conditions of the coils using a network analyzer (ZVB4; Rhode & Schwarz GmbH & Co. KG, Munich, Germany). For loading, the intraoral coils were immersed in a phantom made of distilled water with 2g/l NaCl, and 5g/l $NiSO_4$.

C. MRI Measurements

Loop coil and dipole antenna were interfaced to a clinical 3T MRI system (Prisma Fit, Siemens, Erlangen, Germany) via a custom made Tx/Rx switch [27], [48], and the 4 channel SLR array was connected to the system via commercially available preamplifiers (Stark Contrast, Erlangen, Germany).

To compare the imaging results with the simulations, at first the phantom experiments were performed. A PVC bridge was fabricated and attached to the MRI patient table to fix the intraoral coils in the phantom (see Methods, B. Coil Construction) – the same bridge was later used in the volunteer experiments to fıx the intraoral coils and minimize head motion. The dipole was placed through an opening on the fabric of the flex SLR array to avoid displacement of the flex coil and the phantom.

To compare the transmit efficiency of the intraoral loop and dipole to the system's body resonator, a flip angle mapping measurement using double angle method [49] was performed, where the flexible SLR array was used as the Rx element for all three Tx coils. The flip angle was then converted to B_1^+ value, which is then normalized to the supplied input power as reported by the MRI system.

Then, SNR maps were acquired as described in [50] for loop and dipole in Tx/Rx mode, SLR only, and dipole as Tx and SLR as the extraoral Rx element. A 3D GRE sequence was used (Please see Supplementary Material for full sequence protocol). In vivo measurements were performed with the reference loop coil, the dipole antenna with the best-performing design, SLR array alone, and the SLR array combined with the loop coil and the dipole antenna. For imaging, a 3D spoiled gradient echo (GRE) sequence was used with the following parameters: 0.6 mm-isotropic resolution, α = 20°, TR = 25 ms and TE = 3.14 ms. The FOV could be set as 160 × 160 86.4 mm^3 with 144 slices and the total acquisition time amounted to 4:19 min:s. The panoramic slices were created by using the "Straighten" function [51] of ImageJ, which is a Java based image processing program [52]. To demonstrate the compatibility with short $T2_*$ imaging sequences, an ultra-short TE (UTE) sequence protocol was also implemented with TR = 7.96 ms and TE = 60 μs. The nominal resolution was 0.9 mm-isotropic, FOV was 110 × 110 × 110 mm^3, α = 6°, and 128 points per radial spoke were acquired resulting in a total scan time of 8:41 min:s. Full protocols are available in the Supplementary Material. All measurements were performed in accordance with the institutional guidelines and the local ethical review board (University of Minnesota, Human Research Protection Program, STUDY00005298).

Based on the SAR_{10g} simulation results, the transmit power limits for the RF coil were set such that the corresponding maximum SAR_{10g} value was at least 20-fold less than the input power that generates maximum SAR_{10g} of 10 W/kg (averaged over 10 g tissue and 6 min [53]). Note also that the minimum distance between the volunteers' lips and the closest capacitor, which is the highest local E field, was 14 mm and 37 mm for the loop and the dipole, respectively. Peak 10g-averaged SAR calculator of Sim4Life 5.2 software was used to calculate the spatial-average of SAR with moving constant-mass cubes as recommended in [54]. SAR_{10g} maps and SAR efficiency maps (i.e., B_1^+/SAR in μT $kg^{0.5}/W^{0.5}$) of the loop coil and the dipole are shown in Supporting Information Figs. S11 and S12, respectively for a homogeneous phantom.

III. Results

A. FDTD Simulations

In Fig. 1, the coil designs (a-f) are shown together with transverse (g-l) and coronal (M-R) transmit efficiency B_1^+/P_{in} maps. The loop coil shows a homogeneous field distribution along the coil conductor with an increased B_1^+/P_{in} in the conductor section opposite to the feed port. For dental imaging, axial line profile between [0°–130°] and [230°–360°] are relevant (Fig. 1(b)). In Table I, the maximum B_1^+/P_{in} along the axial profiles at z_1 = 10 mm and z_2 = 25 mm planes, mean absolute deviation along the axial profile, peak B_1^+ along the longitudinal profile at levels y_1 and y_2, and longitudinal variation calculated as $100\left(1\ B_1^+(z_2)/B_1^+(z_1)\right)$ are given. Corresponding line profile plots for planar dipoles, multi-planar dipoles, and multi-planar dipoles with high-ε_r cap are shown in Supporting Information Figs. S4, S5, and S6, respectively.

In Table I, for the planar dipoles, 3-wire designs have the highest B_1^+, yet mean absolute deviation is lowest for the meander dipole. However, due to the near field (observed at transverse planes at $z < 5$ mm) inhomogeneities of the meander dipole (Supporting Information Video S1), this design was left out. 3-wire and ribbon dipoles have comparable deviation and maximum B_1^+ values.

In Fig. 2(f)–(j), transverse B_1^+/P_{in} maps of the multi-plane dipoles are shown, which is superior to the planar dipoles in terms of maximum B_1^+/P_{in}. Unlike the planar 3-wire dipole with shorted ends, 7-wire dipole with shorted ends has a more homogeneous axial profile than other multi-planar designs (Table I). 7-wire dipoles have higher maximum B_1^+/P_{in} values, whereas the ribbon based multi-planar design performs slightly better in terms of longitudinal homogeneity.

The problem of the inhomogeneity along the axial profile is resolved with the addition of a high-ε_r cap, as shown in Table I. According to the simulations, high-ε_r cap of 15 mm length results in a more flat axial profile along the dipole arms (Fig. 4). Fig. 2(k)–(o) shows longitudinal profiles along a plane cutting the 15 mm-long high-permittivity cap at the center. Here 7-wire dipole with high-ε_r cap has higher intensity compared to other 7-wire and ribbon-based multi-planar designs. From Table I, a 7-wire dipole with shorted ends and 15 mm-long high-ε_r cap was selected as the best-performing design as it has slightly higher homogeneity and comparable maximum B_1^+/P_{in} as the open-end design, and was constructed for MRI measurements. Axial and longitudinal line profiles of the selected dipole designs and the loop design are shown in Supporting Information Fig. S7.

SAR_{10g} maps for loop and dipole coil in the Duke anatomical model are shown in Fig. 5. The values are normalized to 0.02W input power, which is calculated from the peak voltage level of the RF pulse used in the measurements. Slices with the highest SAR_{10g} are shown in transverse and coronal planes. The color maps are scaled to the maximum SAR_{10g}. In the

loop coil, power deposition around the feed port is higher than the other regions (Fig. 5(c)–(d)). In the dipole, power deposition increases around the high-ε_r cap of the dipole arms (Fig. 5(a)–(b)). To investigate the effect of the high-ε_r cap further, another set of simulations, where the high-ε_r cap was excluded was performed (Supporting Information Fig. S13). The power deposition was comparable for dipoles with high and low ε_r, i.e., 0.17 W/kg and 0.20 W/kg, respectively. However, the power deposition in low ε_r dipole was higher around the feed port and the sections of the dipole arms close the feed port.

B. Coil Construction

S-parameter measurements are shown in Fig. 3(c). Unloaded and loaded Q factors for loop, dipole, and SLR elements are $Q_{unloaded}/Q_{loaded}$ = 70.8/6.2, 8.2/3.9, 64.5/20.3, respectively. SLR elements and dipole are decoupled by 33±4 dB when positioned as illustrated in Fig. 3(d), and the reflection coefficient of the dipole is not affected from the nearby SLR elements. S-parameter and noise covariance matrices for the SLR array are shown in Figs. 3(e)–(f). The range of coupling between overlapping/non neighboring elements was −21.3–13.5 dB/−18.3–13.5 dB, to which preamplifier decoupling added another 23±5 dB isolation. The active detuning efficiency was measured as 48±4 dB for all elements. Noise correlation values ranged from 3% to 9% (Fig. 3(f)).

C. MRI Measurements

B_1^+ efficiency maps in μT/W are shown in Fig. 6 for the transverse slices 10 mm away from the coil planes. The intraoral dipole and loop have comparable maximum B_1^+ efficiency of 388.2, 384.6, 6.9 μT/W, respectively. The dipole has a smaller excited volume than the loop; however, both intraoral coils have higher B_1^+ efficiency and smaller excitation volume compared to the body resonator of the system.

Transverse slices at z = 10 mm of the phantom images are shown in Supporting Information Fig. S8b–f. Mean SNR in the marked region of interest shown on the images were 271.9/32.3/440.1/861.7/645.7 for the loop, the dipole, SLR only, and the SLR combined with the loop and the dipole, respectively. At z = 20 mm, the SNR values for the SLR combined with loop and dipole are 287.8 and 924.2, respectively, due to the inhomogeneous flip angle distribution along the longitudinal direction.

In Fig. 7(b)–(f), in vivo images of the human mandible are shown in a transverse and a coronal plane. The transverse plane was positioned close to the intraoral coil plane (z = 4 mm), and the SNR values from dentine at the right first molar were measured and found to be 14.8/4.6/40.5/141.7/189.6 for the loop, the dipole, SLR only, and the SLR combined with the loop and the dipole, respectively. The dipole has an inferior SNR when used as a Tx/Rx element, which is expected from the low Q factor. Coronal profiles, on the other hand, show that the dipole combined with SLR has a higher depth–of-sensitivity than the loop, in agreement with the phantom SNR comparison of the transverse planes at z = 10 mm and z = 20 mm. The combination of the dipole with extraoral SLR Rx array improved the SNR without the need for increasing the FOV. Signal from tongue, which can cause unwanted artifacts, was also reduced in the dipole compared to the loop coil. When the intraoral coils

are combined with the extraoral flexible SLR array, there is a signal enhancement around the feed port, close to the phantom surface, which is more noticeable in the dipole and SLR combination (Supporting Information Fig. S8f). A signal enhancement around the feed port is visible also in Fig. 7(f), where image intensity of lips and frontal gums is higher than the other tissue. Note that signal from tongue could not be suppressed completely in the dipole. Line profiles of the contrast-to-noise ratio (CNR) of the tongue to the first molar teeth reveal that the edges of the tongue are still prominent compared to signal at the medial sulcus of the tongue, since the sensitivity of the dipole decreases gradually towards the center of the tongue (Supporting Information Fig. S14).

In the GRE images, the dental restoration in the left first molar is seen as a susceptibility artefact (Fig. 7(f)), which is reduced in the corresponding UTE images (Supporting Information Fig. S9). A panoramic view of the in vivo images acquired using the SLR and dipole combination are shown in Fig. 8. An animated overview covering all the slices of the GRE and UTE images is presented as Supporting Video S2.

IV. Discussion

In this study, a dipole antenna was designed to overcome the limitations of current intraoral coil designs based on loop coils. The results show that a dipole antenna with 7 wires and a high-ε_r cap can be potentially useful in dental MRI at 3 T. Although dipoles have lower SNR compared to loop coils, it was demonstrated that when they are used as a Tx-only element in combination with an extraoral SLR array, SNR can be improved, patient comfort can be improved, and small FOVs can be used with conventional pulse sequence protocols.

From the outset of the coil designs, planar designs with various arm shapes were compared in EM simulations. The multi-wire approach was inspired by UHF antenna designs; however, a unique design was developed to generate a region with homogeneous sensitivity that covers molar teeth. Other unique design features are the use of additional wires around the teeth that extend the depth-of-sensitivity toward the roots, and the use of high-ε_r cap at the tip of the dipole arms. In the comparison, the wire type, the conductivity, the distance between the upper wires and the main arm at the central plane, and the dielectric constant of the high-ε_r cap were not varied. A higher conductivity and a lower wire resistance would lead to a higher Q for the coil but would not substantially change the B_1^+ profiles. The distance between the wires is limited by the oral anatomy. The permittivity is already very high in barium titanate and is difficult to increase with biocompatible materials. Thus, the current comparison should already provide a good approximation for the desired sensitivity profile of the coil. Note that, in the simulations, for an 8.7% change in ε_r, absolute changes are within 2% and 3% B_1^+ and SAR_{10g}, respectively. Therefore, for a substantial modification of the field distribution, materials with substantially higher permittivity should be investigated [55]–[58].

The 3D UTE imaging with $(110\ m)^3$ FOV proves that the coil system with the intraoral dipole as Tx element and the extraoral SLR array as the Rx element can be used with high-resolution radial imaging sequences in vivo. The low Q of the dipole is even advantageous for the ultra-short TE measurements as the Q is proportional to the ring down time. Ring-

down time might be a limiting factor in minimizing the acquisition delay in ultra-short TE sequences such as UTE and SWIFT.

Direct imaging of calcified tissues by using echo-based conventional MRI, such as GRE, is not possible due to the ultrashort relaxation time of transverse magnetization (for enamel, $T2_*$ ~0.07 ms), which is usually shorter than the echo time (TE = 3.1 ms, in this study). However, studies have shown that conventional MRI can be used clinically to visualize, for example, pulp structure and vitality [8], to reveal the anatomy and pathology of the dento-alveolar [59], to detect osteomyelitis in the mandible [60], and to indirectly image highly mineralized tissue through contrast produced by tissue with long relaxation times [10], [40], [59], [61]–[63]. On the other hand, the performances of MRI methods for obtaining images of densely calcified dental tissues with positive contrast such as UTE and SWIFT are still limited by the electronics and digitization chain of the clinical MRI systems. For the UTE images acquired with 0.06 ms echo time, a certain signal is expected from the dentin with $T2_*$ of about 70 μs [27], [64], yet, due to the blurring from rapid decay of magnetization and the high signal intensity of the surrounding tissue, the available contrast is hiding these parts of the teeth. Alternatively, two UTE images acquired with short and long TEs could be subtracted to highlight the densely calcified tissues [65]. Furthermore, patient motion must be addressed in clinical dental imaging by adaptive retrospective correction of motion artefacts when high-resolution imaging of small structures with ultra-short $T2_*$ is desired. MR signal from the intraoral coil housing can also obscure dental tissues. Signal from coil former and insulation materials should either be minimized by using 1H-free compounds or be adjusted using contrast agent mixtures.

In general, the Tx homogeneity of the dipole at 3 T is inferior to a volume coil such as a birdcage or solenoid. However, larger volume coils would also lead to large FOVs and unwanted signal contributions from the tongue and other surrounding structures, so that the combination of the inhomogeneous dipole with an extraoral receive array is still advantageous. The Tx inhomogeneity of the dipole can be partially overcome by using B_1^+ insensitive excitation pulses and encoding methods that improve the homogeneity [29], [66]–[68].

At the feed port, high signal from lips and surrounding tissues can be observed, which might be difficult to remove in clinical imaging. High signal from these spots could be reduced by RF shielding of the field port, or the feed port could be modified to form a strip line, where the electric and magnetic fields are constrained between two grounds, so that the sensitivity to external signals is minimized.

There are several challenges to produce a re-usable intraoral dipole antenna. First, the coil must allow for easy disinfection without damaging the isolation layers. Therefore, the isolating cover needs to be chemically and mechanically more stable than the one used in this prototype implementation. Alternatively, it can be designed as two parts, a dipole part and the circuitry part, that are linked via a connector. The circuitry could be re-usable, whereas the dipole part is disposed after in vivo use, similar to rectal coils for prostate MRI. Another challenge is to reproduce the high-permittivity cap. The current method of filling a hollow H-shaped container with a $BaTiO_3$ slurry is mechanically fragile, and the

wires inside it can be unintentionally bent, which can affect the performance of the coil. In the future, the high-permittivity cap can be made of a non-toxic ceramic or another high-permittivity biocompatible compound.

Human mandibular size and shape can vary depending on several factors including, but not limited to patient age, ethnicity, and gender. Thus, the dipole size is not a free parameter, but must be chosen to fit comfortably inside the mouth and cover the dental arches for proper diagnosis. Dental impression trays, for example, are commonly available in five sizes denoted as XS, S, M, L, and XL, which covers most of the population. A similar range of sizes could also be offered for intraoral coils. Dipole sensitivity is not significantly affected by the size of the arms (see Supporting Information Fig. S10, depth of sensitive region is plot for S, M, and L size coils), so the results of this comparison study can be extended to dipoles with arms that are longer or shorter by about 20%. It is a limitation of the multi-planar dipole design that not only the size, but also the form and the shape of the antenna structure will be determining if the antenna fits the patient's mouth without stressing the tissue, which could be a major source of discomfort during clinically relevant measurement times. To eliminate this effect, development of multi-planar dipole antennae with using flexible conductors and formers are in the scope of future research. To compensate for the tuning and matching offsets in such a flexible arrangement, automated tuning and matching technologies are favorable [69]–[71].

Most of the electric fields generated by the intraoral dipoles are dissipated within the isolating cover and the surrounding tissue. Even if the total power delivered to the coil is low due to the high filling ratio and the choice of the pulse sequence, local E field hot spots might be formed within the mouth, which could lead to unwanted local heating when RF pulses with high peak power are used. High local SAR was observed at the input port of the loop and at the end of the dipole arms as shown in the preliminary SAR simulation results for the loop and dipole models used in the volunteer measurements (Supporting Information Fig. S11). SAR efficiency of the dipole is therefore decreasing towards the end of the dipole arms (Supporting Information Fig. S12). The simulations performed using the Duke anatomical model also revealed similar distribution of power deposition in the tissue.

High-intensity E fields are observed close to the conducting surfaces and capacitors. Although no temperature increase was observed during the MRI measurements in this study, temperature measurements must be performed at these potential hot spots, and, additionally, the design must be locally changed to minimize direct tissue contact before translating this technology to a clinical study. The thickness and material properties of the isolation layer can be optimized to reduce local SAR. E fields around the capacitors and the feed ports can be reduced either by keeping the tissue away from hotspots, or shielding the feed port similar to an embedded coplanar strip line design, which would keep the E fields within the parallel ground planes. Especially for high power demanding sequences, the SAR distribution needs to be optimized. A limitation of this study is that we evaluated only the sensitivity profile of the dipole by simulating dipoles with different lengths of high-ε_r caps. In future studies, the power deposition should be optimized in parallel, to avoid hotspots. A more comprehensive RF safety analysis including thermal simulations with different computational human models and temperature measurements is beyond scope

of this manuscript but needs to be performed before intraoral loop coil and dipole antennae can be used in a larger patient population.

The results of this study might also be interesting for the design of ultra-high field RF coils, as dipoles are frequently used at 7 T and higher field strengths [72], [73]. Although an intraoral coil has a much higher filling factor than dipoles used for body or head MRI, techniques for increasing penetration depth and for improving homogeneity can be adapted to other coils.

Figs. 7 and 8 present the first in vivo MRI images using an intraoral dipole antenna. Combination of a dipole antenna and SLRs were also implemented for the first time, to the best of our knowledge. The spatial resolution can be increased in the expense of acquisition time. Although there is no hardware limit to achieve a higher resolution, the effects of the residual motion and off-resonance blurring needs to be addressed; these can be compensated at the post processing stage for radial acquisition and are in the scope of future research.

We also performed the first SAR simulations for an intraoral coil in an anatomical human model. Intraoral coils needs to be optimized to minimize local power deposition in tissue to extend the range of the applications to power demanding sequences such as RARE [74]. Since the intraoral dipole antenna is set very close to the sensitive organs and tissue such as tongue, RF energy deposition and local SAR values need to be monitored carefully. Limiting the transmit power to ensure safe operation may also limit the maximal flip angle in magnetization prepared and spin-echo-based sequences, which is a critical aspect of the intraoral coils and needs to be addressed in future studies.

V. Conclusion

We demonstrated feasibility of using a dipole antenna as an intraoral coil and improved the transmit efficiency and homogeneity of this coil. The intraoral dipole allows free tongue movement. Transmission efficiency of the intraoral loop and dipole are similar within 15 mm distance to the coil planes, however, dipole outperforms the loop when the distance is larger than 20 mm. The combination of the intraoral dipole and the extraoral SLR Rx array is required to achieve SNR comparable to or higher than the loop coil.

Supplementary Material

Refer to Web version on PubMed Central for supplementary material.

Acknowledgment

The authors are thankful to CMRR scientists and faculty for their help, especially to R. Lagore, J. Radder, Y. Eryaman, A. Sadeghi-Tarakameh, A. Grant, and J. Thotland. We also thank J. Fischer and S. Ilbey of University Medical Center Freiburg for their help with the measurement setup.

The work of Ali Caglar Özen was supported by the School of Dentistry of UMN’s Lasby Fellowship and in part by the Biomedical Technology Resource Center (BTRC) grant NIH (P41 EB025144).

References

[1]. Vandenberghe B et al. , “Modern dental imaging: A review of the current technology and clinical applications in dental practice,” Eur. Radiol, vol. 20, no. 11, pp. 2637–2655, Nov. 2010. [PubMed: 20544352]

[2]. Pauwels R et al. , “Technical aspects of dental CBCT: State-of-the-art,” Dentomaxillofacial Radiol., vol. 44, no. 1, Jan. 2015, Art. no. 20140224.

[3]. Masthoff M et al. , “Dental imaging – a basic guide for the radiologist,” RöFo - Fortschritte Auf Dem Gebiet der Röntgenstrahlen Und Der Bildgeb. Verfahren, vol. 191, no. 03, pp. 192–198, Mar. 2019.

[4]. van Luijk JA, “NMR: Dental imaging without x-rays?” Oral Surg., Oral Med. Oral Pathol, vol. 52, no. 3, pp. 321–324, Sep. 1981. [PubMed: 6945543]

[5]. Lam EWN et al. , “Imaging orofacial tissues by magnetic resonance,” Oral Surg., Oral Med. Oral Pathol, vol. 68, no. 1, pp. 2–8, Jul. 1989. [PubMed: 2755685]

[6]. Chen YJ et al. , “Dynamic magnetic resonance imaging technique for the study of the temporomandibular joint,” J. Orofac. Pain, vol. 14, no. 1, pp. 65–73, 2000. [Online]. Available: http://www.ncbi.nlm.nih.gov/pubmed/11203741 [PubMed: 11203741]

[7]. Gray CF et al. , “Advanced imaging: Magnetic resonance imaging in implant dentistry. A review,” Clin. Oral Implants Res, vol. 14, no. 1, pp. 18–27, Feb. 2003. [PubMed: 12562361]

[8]. Kress B et al. , “Quantitative analysis of MRI signal intensity as a tool for evaluating tooth pulp vitality,” Dentomaxillofacial Radiol, vol. 33, no. 4, pp. 241–244, Jul. 2004.

[9]. Larheim TA, “Role of magnetic resonance imaging in the clinical diagnosis of the temporomandibular joint,” Cells Tissues Organs, vol. 180, no. 1, pp. 6–21, 2005. [PubMed: 16088129]

[10]. Ferretti F et al. , “Dental magnetic resonance imaging: Study of impacted mandibular third molars,” Dentomaxillofacial Radiol, vol. 38, no. 6, pp. 387–392, Sep. 2009.

[11]. Tymofiyeva O et al. , “Three-dimensional localization of impacted teeth using magnetic resonance imaging,” Clin. Oral Investig, vol. 14, no. 2, pp. 169–176, Apr. 2010.

[12]. Gaudino C et al. , “MR-Imaging of teeth and periodontal apparatus: An experimental study comparing high-resolution MRI with MDCT and CBCT,” Eur. Radiol, vol. 21, no. 12, pp. 2575–2583, Dec. 2011. [PubMed: 21805369]

[13]. Vidmar J et al. , “Assessment of the dentin-pulp complex response to caries by ADC mapping,” NMR Biomed, vol. 25, no. 9, pp. 1056–1062, Sep. 2012. [PubMed: 22246979]

[14]. Tymofiyeva O et al. , “Diagnosis of dental abnormalities in children using 3-Dimensional magnetic resonance imaging,” J. Oral Maxillofac. Surg, vol. 71, no. 7, pp. 1159–1169, Jul. 2013. [PubMed: 23611603]

[15]. Assaf AT et al. , “Early detection of pulp necrosis and dental vitality after traumatic dental injuries in children and adolescents by 3-Tesla magnetic resonance imaging,” J. Cranio-Maxillofac. Surg, vol. 43, no. 7, pp. 1088–1093, Sep. 2015.

[16]. Singer SR and Creanga AG, “Diagnostic imaging of malignant tumors in the orofacial region,” Dent. Clin. North Amer, vol. 60, no. 1, pp. 143–165, Jan. 2016. [PubMed: 26614953]

[17]. Niraj LK et al. , “MRI in dentistry—A future towards radiation free imaging – systematic review,” J. Clin. Diagn. Res, vol. 10, no. 10, pp. ZE14–ZE19, 2016.

[18]. Boeddinghaus R and Whyte A, “Trends in maxillofacial imaging,” Clin. Radiol, vol. 73, no. 1, pp. 4–18, 2018. [PubMed: 28341434]

[19]. Hilgenfeld T et al. , “High-resolution dental magnetic resonance imaging for planning palatal graft surgery-a clinical pilot study,” J. Clin. Periodontol, vol. 45, no. 4, pp. 462–470, Apr. 2018. [PubMed: 29334405]

[20]. Kocasarac HD et al. , “MRI for dental applications,” Dent. Clin. North Amer, vol. 62, no. 3, pp. 467–480, 2018. [PubMed: 29903562]

[21]. Idiyatullin D et al. , “Role of MRI for detecting micro cracks in teeth,” Dentomaxillofacial Radiol, vol. 45, no. 7, 2016.

[22]. Weiger M et al. , “High-resolution ZTE imaging of human teeth,” NMR Biomed, vol. 25, no. 10, pp. 1144–1151, 2012. [PubMed: 22290744]

[23]. Bydder GM, “The agfa mayneord lecture: MRI of short and ultrashort T2and T2* components of tissues, fluids and materials using clinical systems,” Br. J. Radiol, vol. 84, no. 1008, pp. 1067–1082, 2011. [PubMed: 22101579]

[24]. Robson MD and Bydder GM, “Clinical ultrashort echo time imaging of bone and other connective tissues,” NMR Biomed, vol. 19, no. 7, pp. 765–780, 2006. [PubMed: 17075960]

[25]. Tyler DJ et al. , “Magnetic resonance imaging with ultrashort TE (UTE) PULSE sequences: Technical considerations,” J. Magn. Reson. Imag, vol. 25, no. 2, pp. 279–289, Feb. 2007.

[26]. Weiger M et al. , “{MRI} with zero echo time: Hard versus sweep pulse excitation,” Magn. Reson. Med, vol. 66, no. 2, pp. 379–389, 2011. [PubMed: 21381099]

[27]. Özen AC et al. , “Comparison of ultrashort echo time sequences for MRI of an ancient mummified human hand,” Magn. Reson. Med, vol. 75, no. 2, pp. 701–708, Feb. 2016. [PubMed: 25752671]

[28]. Garwood M, “MRI of fast-relaxing spins,” J. Magn. Reson, vol. 229, no. 0, pp. 49–54, Apr. 2013. [PubMed: 23465800]

[29]. Idiyatullin D et al. , “Fast and quiet MRI using a swept radiofrequency,” J. Magn. Reson, vol. 181, no. 2, pp. 342–349, Aug. 2006. [PubMed: 16782371]

[30]. Idiyatullin D et al. , “Multi-band-SWIFT,” J. Magn. Reson, vol. 251, pp. 19–25, Feb. 2015. [PubMed: 25557859]

[31]. Idiyatullin D et al. , “Continuous SWIFT,” J. Magn. Reson, vol. 220, no. April, pp. 26–31, Jul. 2012. [PubMed: 22683578]

[32]. Özen AC et al. , “Active decoupling of RF coils using a transmit array system,” Magn. Reson. Mater. Phys., Biol. Med, vol. 28, no. 6, pp. 565–576, Dec. 2015.

[33]. Sohn S-M et al. , “In vivo MR imaging with simultaneous RF transmission and reception,” Magn. Reson. Med, vol. 76, no. 6, pp. 1932–1938, Dec. 2016. [PubMed: 27670251]

[34]. Özen AC et al. , “In vivo MRI with concurrent excitation and acquisition using automated active analog cancellation,” Sci. Rep, vol. 8, no. 1, Jul. 2018, Art. no. 10631. [PubMed: 30006628]

[35]. Macovski A, “Noise in MRI,” Magn. Reson. Med, vol. 36, no. 3, pp. 494–497, Sep. 1996. [PubMed: 8875425]

[36]. Hoult DI and Richards RE, “The signal-to-noise ratio of the nuclear magnetic resonance experiment,” J. Magn. Reson, vol. 24, no. 1, pp. 71–85, Oct. 1976.

[37]. Bracher A-K et al. , “Ultrashort echo time (UTE) MRI for the assessment of caries lesions,” Dentomaxillofacial Radiol., vol. 42, no. 6, pp. 20120321, Jun. 2013.

[38]. Prager M et al. , “Dental MRI using a dedicated RF-coil at 3 Tesla,” J. Cranio-Maxillofac. Surg, vol. 43, no. 10, pp. 2175–2182, Dec. 2015.

[39]. Sedlacik J et al. , “Optimized 14+1 receive coil array and position system for 3D high-resolution MRI of dental and maxillomandibular structures,” Dentomaxillofacial Radiol., vol. 45, no. 1, pp. 2–7, 2015.

[40]. Tymofiyeva O et al. , “In vivo MRI-based dental impression using an intraoral RF receiver coil,” Concepts Magn. Reson. Part B Magn. Reson. Eng, vol. 33B, no. 4, pp. 244–251, Oct. 2008.

[41]. Idiyatullin D et al. , “Dental magnetic resonance imaging: Making the invisible visible,” J. Endod, vol. 37, no. 6, pp. 745–752, Jun. 2011. [PubMed: 21787482]

[42]. Ludwig U et al. , “Dental MRI using wireless intraoral coils,” Sci. Rep, vol. 6, no. 1, Mar. 2016, Art. no. 23301. [PubMed: 27021387]

[43]. Idiyatullin D et al. , “Intraoral approach for imaging teeth using the transverse b 1 field components of an occlusally oriented loop coil,” Magn. Reson. Med, vol. 72, no. 1, pp. 160–165, Jul. 2014. [PubMed: 23900995]

[44]. Raberin M et al. , “Dimensions and form of dental arches in subjects with normal occlusions,” Am J. Orthod Dentofac. Orthop, vol. 104, no. 1, pp. 67–72, 1993.

[45]. Sadeghi-Tarakameh A et al. , “A new coil element for highly-dense transmit arrays : An introduction to non-uniform dielectric substrate (NODES) antenna,” in Proc. Intl. Soc. Mag. Res. Med, 2019, pp. 732.

[46]. Eryaman Y et al. , “Combined loop + dipole arrays for 7 T brain imaging,” in Proc. Intl. Soc. Mag. Reson. Med, 2013, pp. 393.

[47]. Ertürk MA et al. , “A 16-channel combined loop-dipole transceiver array for 7 Tesla body MRI,” Magn. Reson. Med, vol. 77, no. 2, pp. 884–894, Feb. 2017. [PubMed: 26887533]

[48]. Özen AC, “Novel MRI technologies for structural and functional imaging of tissues with Ultrashort T 2 values,” 2017, doi: 10.5445/KSP/1000068880.

[49]. Insko EK and Bolinger L, “Mapping of the radiofrequency field,” J. Magn. Reson. Ser. A, vol. 103, no. 1, pp. 82–85, Jun. 1993.

[50]. Henkelman RM, “Measurement of signal intensities in the presence of noise in MR images,” Med. Phys, vol. 12, no. 2, pp. 232, 1985. [PubMed: 4000083]

[51]. Kocsis E et al. , “Image averaging of flexible fibrous macromolecules: The clathrin triskelion has an elastic proximal segment,” J. Struct. Biol, vol. 107, no. 1, pp. 6–14, Aug. 1991. [PubMed: 1817611]

[52]. Collins TJ, “ImageJ for microscopy,” Biotechniques, vol. 43, no. 1S, pp. S25–S30, Jul. 2007.

[53]. IEC. Part 2–33: Particular requirements for the basic safety and essential performance of magnetic resonance equipment for medical diagnosis. 3.2. CSV; 2015. Medical electrical equipment. IEC 60601-2-33:2010+AMD1:2013+AMD2:2015.

[54]. IEC/IEEE, “IEC/IEEE 62704.1:2017 - Determining the peak spatial-average specific absorption rate (SAR) in the human body from wireless communications devices, 30 MHz to 6 GHz,” Part 1: General requirements for using the finite difference time-domain (FDTD) method for SAR calculations.

[55]. Zivkovic I et al. , “High permittivity ceramics improve the transmit field and receive efficiency of a commercial extremity coil at 1.5 Tesla,” J. Magn. Reson, vol. 299, pp. 59–65, Feb. 2019. [PubMed: 30580045]

[56]. Chen W et al. , “Tunable ultrahigh dielectric constant (tuHDC) ceramic technique to largely improve RF coil efficiency and MR imaging performance,” IEEE Trans. Med. Imag, vol. 39, no. 10, pp. 3187–3197, Oct. 2020.

[57]. Koolstra K et al. , “Improved image quality and reduced power deposition in the spine at 3 T using extremely high permittivity materials,” Magn. Reson. Med, vol. 79, no. 2, pp. 1192–1199, Feb. 2018. [PubMed: 28543615]

[58]. Rupprecht S et al. , “Improvements of transmit efficiency and receive sensitivity with ultrahigh dielectric constant (uHDC) ceramics at 1.5 T and 3 T,” Magn. Reson. Med, vol. 79, no. 5, pp. 2842–2851, May 2018. [PubMed: 28948637]

[59]. Tutton LM and Goddard PR, “MRI of the teeth,” Br. J. Radiol, vol. 75, no. 894, pp. 552–562, Jun. 2002. [PubMed: 12124246]

[60]. Lee K et al. , “Magnetic resonance imaging of normal and osteomyelitis in the mandible: Assessment of short inversion time inversion recovery sequence,” Oral surgery, Oral Med. Oral Pathol. Oral Radiol. Endodontol, vol. 96, no. 4, pp. 499–507, Oct. 2003.

[61]. Lockhart PB et al. , “Magnetic resonance imaging of human teeth,” J. Endod, vol. 18, no. 5, pp. 237–244, May 1992. [PubMed: 1402579]

[62]. Olt S and Jakob PM, “Contrast-enhanced dental MRI for visualization of the teeth and jaw,” Magn. Reson. Med, vol. 52, no. 1, pp. 174–176, Jul. 2004. [PubMed: 15236382]

[63]. Węglarz WP et al. , “3D MR imaging of dental cavities—An in vitro study,” Solid State Nucl. Magn. Reson, vol. 25, no. 1–3, pp. 84–87, Jan. 2004. [PubMed: 14698391]

[64]. Tesfai A et al. , “Multi-parameter analytical method for B1 and SNR analysis: (MAMBA): An open source RF coil design tool for short T2*,” J. Magn. Reson, 2020, doi: 10.1016/j.jmr.2020.106825.

[65]. Du J et al. , “Short T2 contrast with three-dimensional ultrashort echo time imaging,” Magn. Reson. Imag, vol. 29, no. 4, pp. 470–482, May 2011.

[66]. Snyder ALS et al. , “MRI by steering resonance through space,” Magn. Reson. Med, pp. 1–10, Aug. 2013.

[67]. De Graaf RA and Nicolay K, “Adiabatic rf pulses: Applications toin vivo NMR,” Concepts Magn. Reson, vol. 9, no. 4, pp. 247–268, 1997.

[68]. Tannús A and Garwood M, “Adiabatic pulses,” NMR Biomed, vol. 10, no. 8, pp. 423–434, Dec. 1997. [Online]. Available: http://www.ncbi.nlm.nih.gov/pubmed/9542739 [PubMed: 9542739]

[69]. Muftuler LT et al. , “Automatic tuned MRI RF coil for multinuclear imaging of small animals at 3T,” J. Magn. Reson, vol. 155, no. 1, pp. 39–44, Mar. 2002. [PubMed: 11945031]

[70]. Venook RD et al. , “Automatic tuning of flexible interventional RF receiver coils,” Magn. Reson. Med, vol. 54, no. 4, pp. 983–993, Oct. 2005. [PubMed: 16155871]

[71]. Sohn SM et al. , “Design of an electrically automated RF transceiver head coil in MRI,” IEEE Trans. Biomed. Circuits Syst, vol. 9, no. 5, pp. 725–732, Oct. 2015. [PubMed: 25361512]

[72]. Raaijmakers AJE et al. , “Design of a radiative surface coil array element at 7 T: The single-side adapted dipole antenna,” Magn. Reson. Med, vol. 66, no. 5, pp. 1488–1497, Nov. 2011. [PubMed: 21630342]

[73]. Sadeghi-Tarakameh A et al. , “In vivo human head MRI at 10.5T: A radiofrequency safety study and preliminary imaging results,” Magn. Reson. Med, vol. 84, no. 1, pp. 484–496, Jul. 2020. [PubMed: 31751499]

[74]. Hennig J et al. , “RARE imaging: A fast imaging method for clinical mR,” Magn. Reson. Med, vol. 3, no. 6, pp. 823–833, Dec. 1986. [PubMed: 3821461]

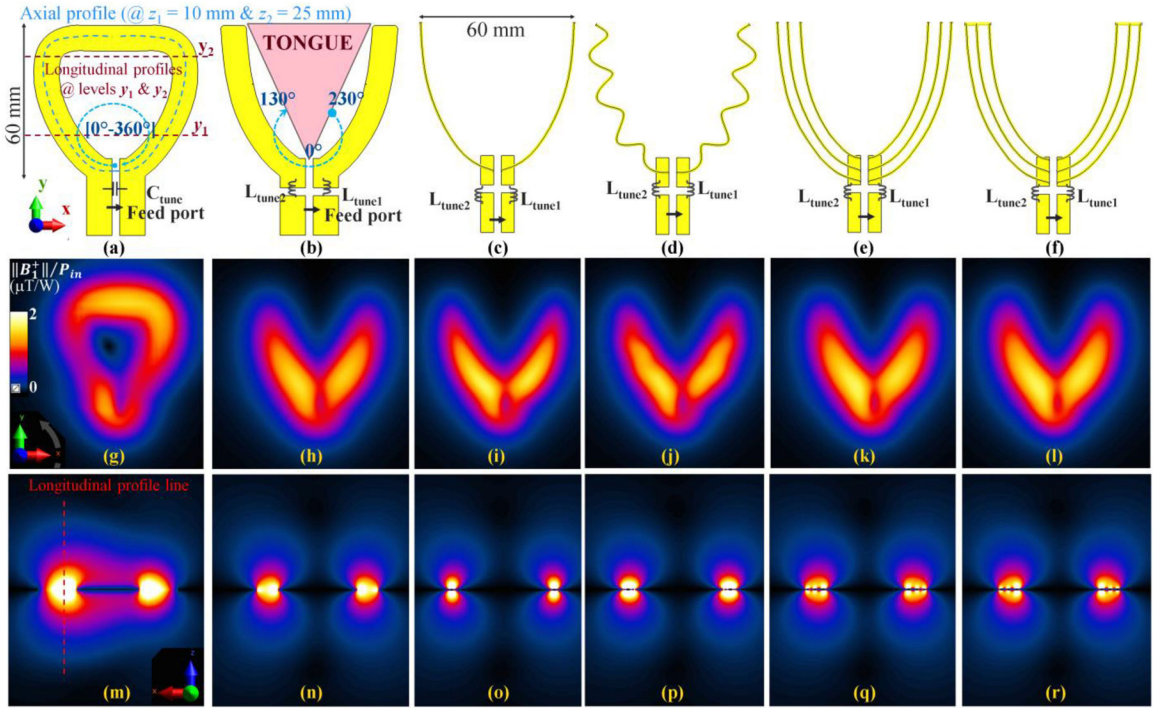

Fig. 1.

Comparison of the intraoral loop and planar dipole coils. (a) Reference loop coil model with the line profile tracks and levels marked. Planar dipole models with (b) ribbon arms, (c) wire arms, (d) meandered wire arms, (e) 3-wire arms, and (f) 3-wire arms with shorted ends. Corresponding field maps are shown in the same column as the coil models. (g)–(h) Sensitivity within the tongue region is lower in dipoles compared to the loop coil. (m)–(r) Ribbon and multi-wire conductors result in a wider sensitivity across the dipole arms.

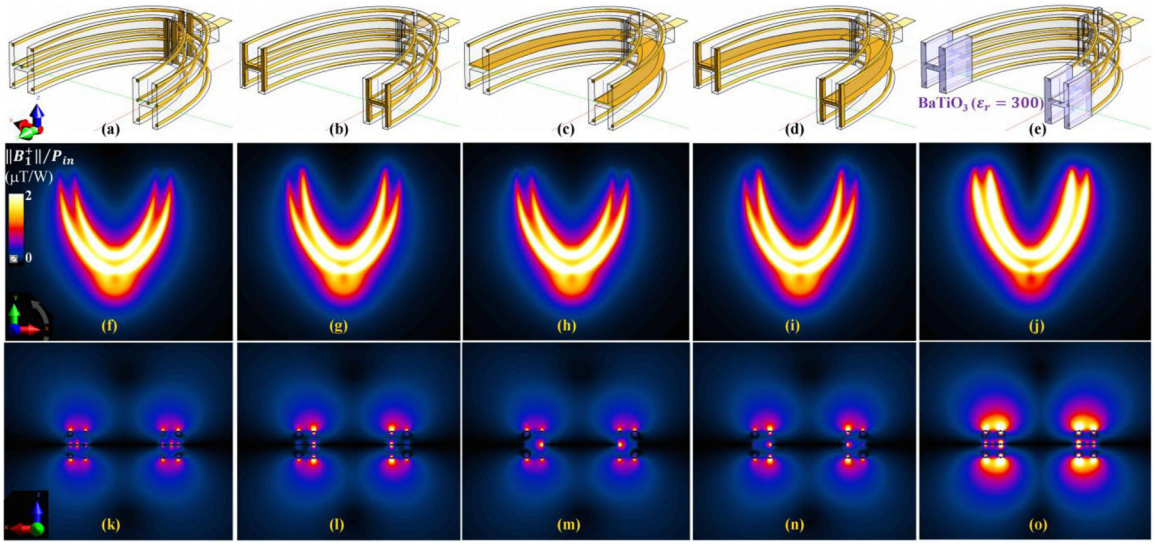

Fig. 2.

Multi-planar dipole models and corresponding field maps. (a) 7-wire, (b) 7-wire with shorted ends, (c) ribbon-based, (d) ribbon-based with shorted ends, and (e) 7-wire dipole with high-ε_r cap. Corresponding field maps are shown in the same column as the coil models. (f)–(j) High-permittivity cap at the end of the dipole arms results in a more homogeneous sensitivity distribution along the arms. (k)–(o) Fields on the coronal slice at the end of the dipole arm also shows the superior performance of the multi-planar dipole with high-permittivity cap in transmit efficiency and homogeneity.

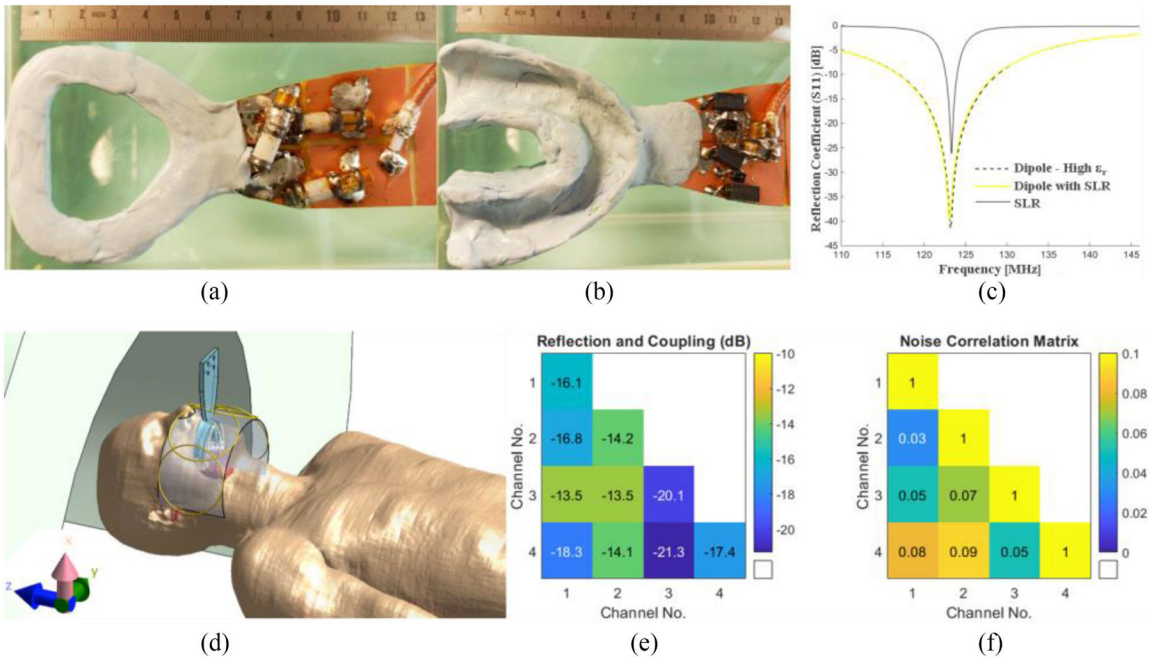

Fig. 3.

A photo of (a) the reference loop coil, (b) 7-wire dipole with shorted ends and high ε_r cap (not visible), and (c) the S-parameter measurements. (d) An illustration of the coil positioning for dipole combined with SLR array, (e) S-parameter and (f) Noise correlation matrices of the SLR array.

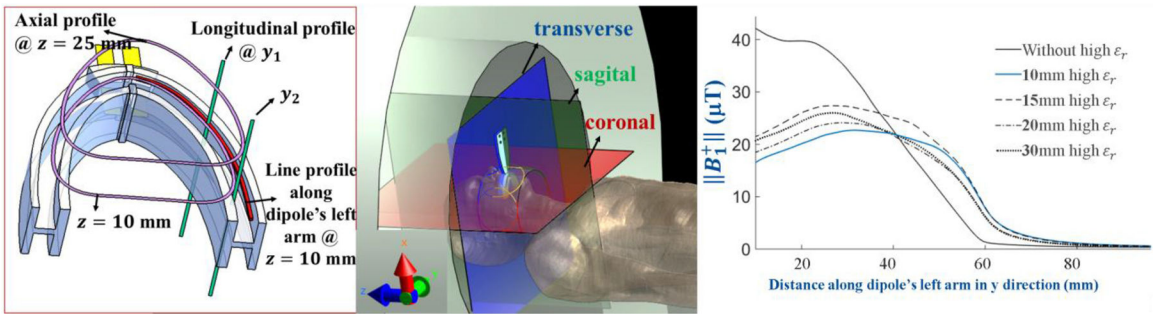

Fig. 4.

Line profile comparison along the dipole arm for different lengths of the high-permittivity cap at the end of the multi-planar 7-wire dipole arm shows that the field homogeneity along the dipole arm can be improved by adjusting the length of the high-permittivity cap.

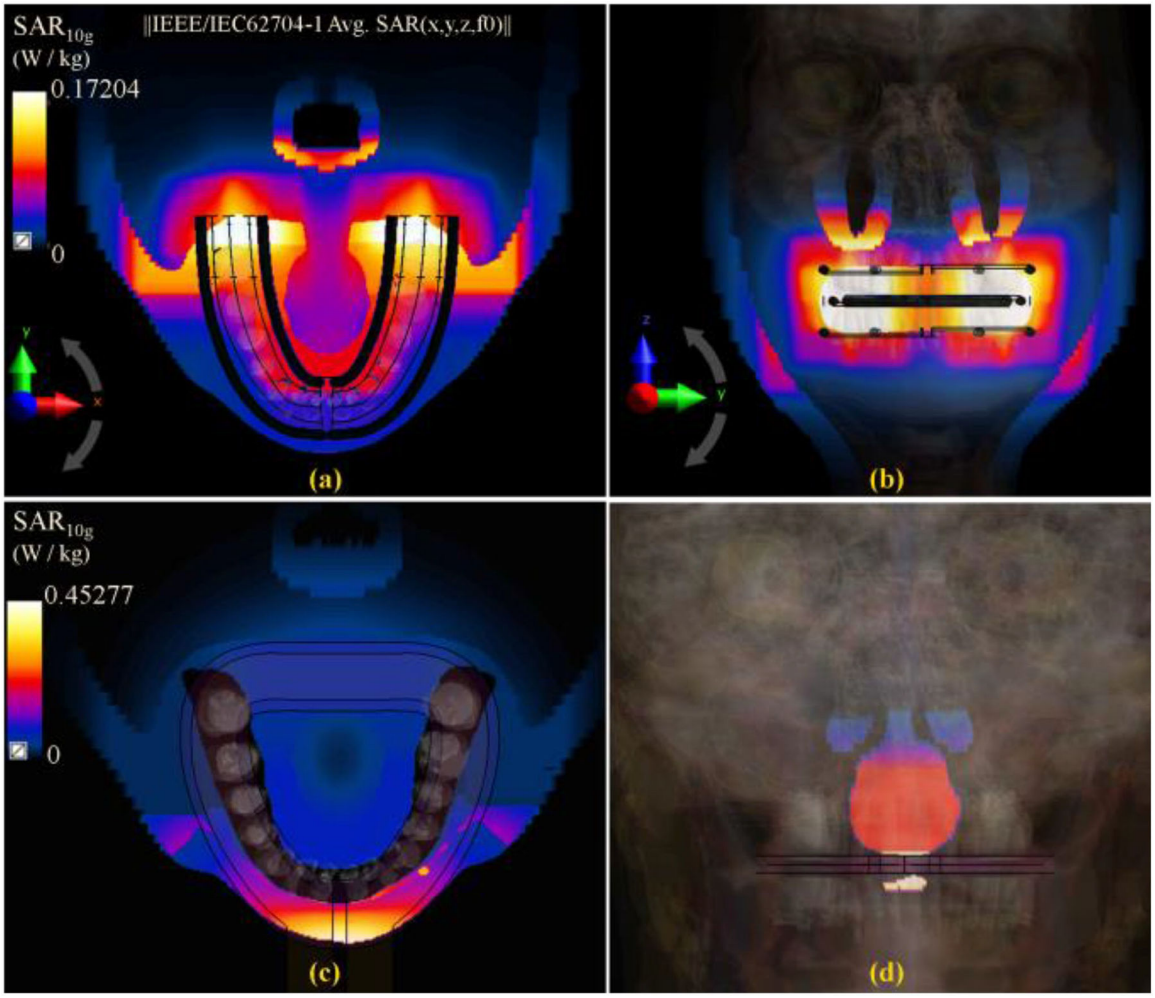

Fig. 5.

SAR_{10g} maps in Duke anatomical model for the intraoral dipole in (a) transverse and (b) coronal planes. SAR_{10g} maps for the intraoral loop in (c) transverse and (d) coronal planes – highest SAR is observed around the lips. The planes are selected with the maximum values; and the color bars represent also the dynamic range of the SAR_{10g} results. Local SAR tends to increase around the feed ports and the high-permittivity cap.

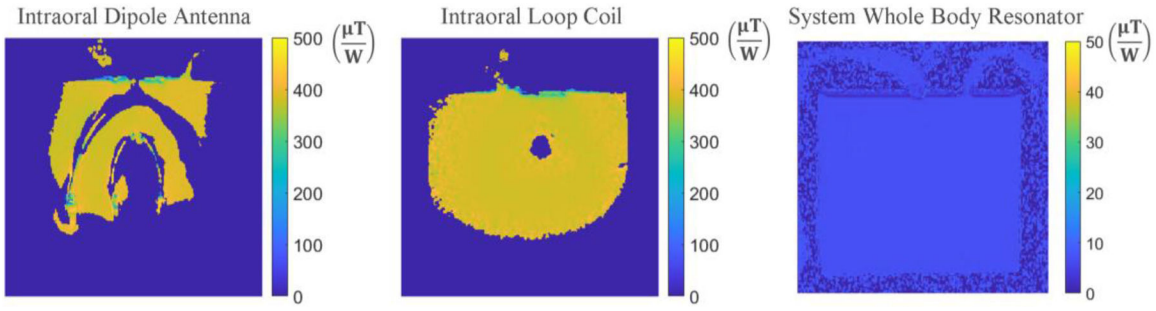

Fig. 6.

Measured B_1^+ efficiency of the intraoral dipole (left), loop (center) and system's body resonator (right) normalized to the output power of the RFPA. As expected, local coils are more efficient than the body coil. Dipole sensitivity drops significantly towards the back and at the medial sulcus of the tongue.

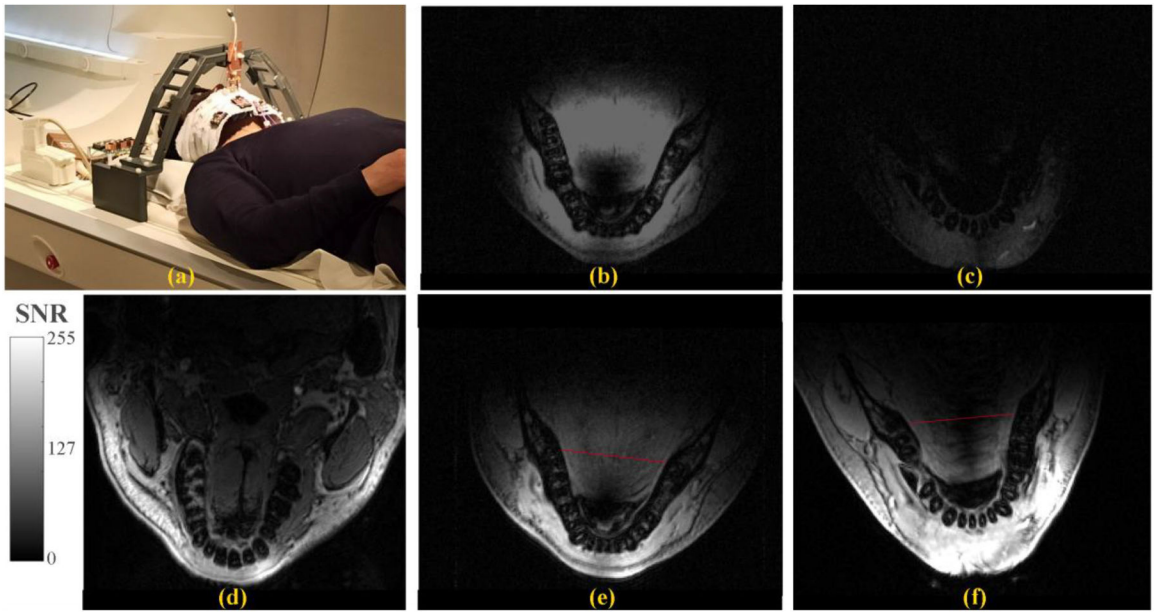

Fig. 7.

A photo of the in vivo measurement setup (a). SNR maps at $z = 10$ mm away from the coil planes for intraoral (b) loop, (c) dipole, (d) extraoral SLR only, and SLR combined with (e) loop and (f) dipole in Tx mode. The image intensities are scaled to the same range to allow a visual SNR comparison. SLR combined with the intraoral dipole provides higher SNR and less signal from the central region of the tongue.

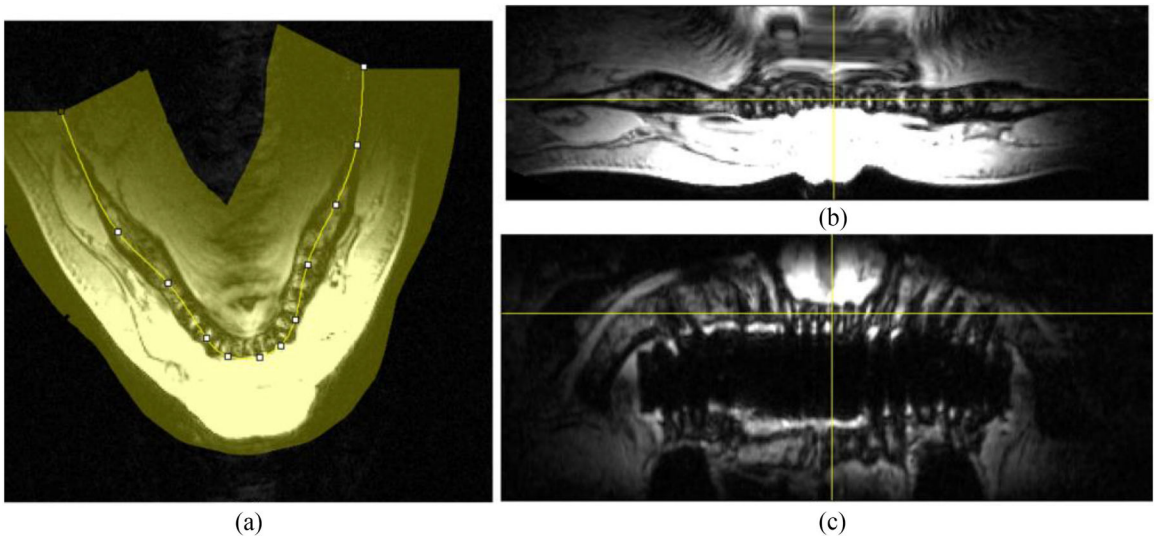

Fig. 8.

A panoramic view of the in vivo GRE images acquired using the SLR and dipole combination. Yellow line shows the cross-section of the folding plane (a). Dipole's sensitivity reaches the roots as shown in the coronal view (c).

Table I

Results of the Line Profile Comparison for Simulations of 13 Dipole Antenna Designs and the Reference Loop Coil Design. Values That Represent the Intensity Are Color-Coded With Green, Whereas the Inhomogeneity, i.e., Deviation of the Intensity, Is Rated With Red Color Scale. The Columns Are Grouped Into Two for Color Coding

Coil Form		Maximum $\|B_1^+\|/P_{in}$ along axial profile (μT/W)		$\|B_1^+\|/P_{in}$ mean absolute deviation along axial profile (%)		Peak $\|B_1^+\|/P_{in}$ along longitudinal profile (μT/W), $\|B_1^+(z = 11\,mm)\|$ for multi-planar		$\|B_1^+\|/P_{in}$ variation along longitudinal profile, i.e., $100 * (1 - \|B_1^+(z_2)\|/\|B_1^+(z_1)\|)$	
		z_1 = 10 mm	z_2 = 25 mm	z_1 = 10 mm	z_2 = 25 mm	y_1	y_2	y_1	y_2
Planar coils	Loop	1.453	0.512	9.7	14.6	0.735	0.928	76.9	70.5
	Ribbon	1.680	0.531	17.8	14.4	1.482	0.774	66.1	62.6
	Wire	1.703	0.497	18.8	15.6	1.510	0.724	69.4	64.4
	Meander	1.620	0.477	17.4	13.7	1.423	0.755	68.2	64.7
	3 wire	1.692	0.531	17.4	14.6	1.455	0.762	65.8	62.2
Multi-planar dipoles	3 wire-short	1.687	0.539	17.3	14.6	1.477	0.787	65.7	62.1
	7 wire	1.718	0.736	21.3	19.7	1.377	0.608	53.8	49.2
	7 wire short	1.678	0.734	16.8	17.2	1.373	0.762	52.3	52.8
	Ribbon	1.667	0.725	21.2	19.7	1.322	0.600	52.7	49.4
	Ribbon-short	1.661	0.731	16.5	17.2	1.361	0.772	52.1	53.6
Multi-planar dipoles with high ε_r	7 wire	2.589	0.778	4.9	8.1	1.605	1.507	52.9	60.9
	7 wire short	2.565	0.787	4.8	7.8	1.638	1.527	53.5	60.2
	Ribbon	2.487	0.773	5.0	8.1	1.602	1.484	53.2	61.0
	Ribbon-short	2.526	0.786	4.9	7.8	1.636	1.507	53.6	60.2